

# Numerical Investigation of Rayleigh-Bénard-Poiseuille Instability in Plane Channel Flow

M. K. Hasan\* and A. Gross<sup>†</sup>

Mechanical and Aerospace Engineering Department, New Mexico State University, Las Cruces, NM 88003

For plane channel flow, thermal stratification resulting from a wall-normal temperature gradient together with an opposing gravitational field can lead to buoyancy-driven instability of three-dimensional waves. Moreover, viscosity-driven instability can lead to the amplification of two-dimensional Tollmien-Schlichting waves. Temporal stability simulations considering different combinations of Reynolds number and Rayleigh number were performed to investigate both the buoyancy and viscosity-driven instability of Rayleigh-Bénard-Poiseuille flow. The investigated cases are either (1) stable, (2) unstable with respect to three-dimensional waves (buoyancy-driven instability), or (3) unstable with respect to two-dimensional waves (viscosity-driven instability). Two new and highly accurate computational fluid dynamics codes have been developed for solving the full and linearized unsteady compressible Navier-Stokes equations in Cartesian coordinates. The codes employ fifth-order-accurate upwind-biased compact finite differences for the convective terms and fourth-order-accurate compact finite differences for the viscous terms. For the case with buoyancy-driven instability, strong linear growth is observed for a broad range of spanwise wavenumbers and the wavelength of the spanwise mode with the strongest nonlinear growth is gradually decreasing in time. For the case with viscosity-driven instability, the linear growth rates are lower and the first mode to experience non-linear growth is a higher harmonic with half the wavelength of the primary wave. The present results are consistent with the neutral curves from the linear stability theory analysis by Gage and Reid.

## I. Introduction

Plane channel flow between two horizontal parallel plates with temperature gradient in the wall-normal direction and gravitational field is known as Rayleigh-Bénard-Poiseuille (RBP) flow. Plane RBP flows have gained much attention because they occur in many engineering applications. The focus has been particularly on the practical consequences of RBP instability for applications such as solar chimney power plants, <sup>1,2</sup> the cooling of electronic components, <sup>3–5</sup> and chemical vapor deposition reactors <sup>6–9</sup> and many others. For RBP flows, both buoyancy and viscosity-driven instability can occur. <sup>10–14</sup> The onset of flow instability is governed by two dimensionless numbers which are the Reynolds number,

$$Re = \frac{u_{max}h/2}{\nu},\tag{1}$$

with maximum velocity,  $u_{max}$ , channel height, h, and kinematic viscosity,  $\nu$ , and the Rayleigh number,

$$Ra = \frac{gh^3\gamma\Delta T}{\nu\alpha}\,, (2)$$

with gravitational acceleration, g, volumetric thermal expansion coefficient,  $\gamma$ , temperature difference,  $\Delta T$ , and thermal diffusivity,  $\alpha$ .

The hydrodynamic stability of RBP flows has attracted considerable attention in the scientific literature over many years. The influence of heterogeneity (stratification) on the hydrodynamic stability of

<sup>\*</sup>Graduate Research Assistant. Member AIAA.

<sup>&</sup>lt;sup>†</sup>Assistant Professor. Senior Member AIAA.

incompressible, inviscid, parallel shear flows has been investigated by Miles. 11 Pearlstein 22 analyzed the two-dimensionality of disturbances for plane RBP flow and found that the most unstable disturbances are either two-dimensional (2-D) transverse or three-dimensional (3-D) longitudinal modes. Ng and Reid<sup>13</sup> performed an investigation of the combined effect of viscosity and stratification on plane channel flow. Fujimura and Kelly<sup>14</sup> employed a weakly nonlinear expansion approach to analyze the nonlinear interaction between longitudinal and transverse flow structures near the Reynolds and Rayleigh number for which both of them become unstable. The linear temporal stability of plane RBP flows was first investigated by Gage and Reid.<sup>10</sup> The neutral curves for the onset of both buoyancy (critical Rayleigh number,  $Ra_c=1,708$ ) and viscosity-driven (Tollmien-Schlichting) instability (critical Reynolds number,  $Re_c = 5,400$ ) were established. When the Reynolds number is below  $Re_c=5{,}400$  and the Rayleigh number is above  $Ra_c=1{,}708$ , buoyancydriven instability occurs and 3-D waves with a wave angle of 90deg are most amplified. For  $Re > Re_c$  and  $Ra < Ra_c$  viscosity-driven instability arises and two-dimensional (2-D) Tollmien-Schlichting (T-S) waves with a wave angle of 0deg are most amplified. The results of the linear stability theory (LST) analyses of plane RBP flow by Gage and Reid<sup>10</sup> were confirmed by numerous computational and experimental investigations. The instability of an unstably stratified plane RBP flow was analyzed by Fujimura and Kelly. <sup>15</sup> For a certain low Reynolds number range  $(0.01 \le Re \le 100)$ , they observed that the critical Rayleigh number for 2-D unstable waves increased with Reynolds number. This finding is essentially consistent with the 0deg neutral curve by Gage and Reid. 10 Akiyama et al. 16 carried out experiments of fully developed laminar plane RBP flow for investigating the development of longitudinal vortices due to buoyancy-driven instability for different wall-normal temperature gradients. An experimental and theoretical investigation of the effect of longitudinal vortex rolls on the transport processes in laminar channel flow (both horizontal and inclined) has been carried out by Fukui and Nakajima.<sup>17</sup> Hasan and Gross<sup>18</sup> performed spatial stability simulations to investigate the buoyancy-driven instability of inward radial RBP flows. The spatial growth rates of 3-D modes were found to vary significantly in the radial direction.

For the stability analyses the spanwise direction is typically considered to be homogeneous such that a wave ansatz with spanwise wavenumber,  $\beta$ , can be employed. This assumption is valid for radial flows (which are periodic in the circumferential direction) but not for square channel flows which do necessarily have a finite aspect ratio. For that reason, some researchers considered square channels with finite lateral extent. Luijkx et al. 19 investigated the stability of a RBP flow in a finite aspect ratio channel and reported that for low Reynolds numbers ( $Re < Re_c$ ), transverse rolls that are aligned perpendicular to the flow direction become dominant over longitudinal rolls. A linear stability analysis by Nicolas et al.<sup>20</sup> revealed that decreasing the lateral extent of the channel has a stabilizing effect on the flow. As long as the Rayleigh number is above critical, transverse rolls are prevalent for Reynolds numbers below the critical Reynolds number and longitudinal flow structures appear for  $Re > Re_c$ . They also investigated RBP flows with infinite aspect ratio and found that the critical Rayleigh number for 2-D transverse waves increases with Reynolds number which is in agreement with Gage and Reid. 10 An experimental investigation of the stability of RBP flows by Grandjean and Monkewitz<sup>21</sup> demonstrated that even for large spanwise aspect ratios, transverse rolls developed when the instability changed from convective to absolute. Mori and Uchida<sup>22</sup> carried out an experimental analysis of fully developed high aspect ratio channel flows and showed that vortex rolls that are aligned parallel with the flow direction appear when the temperature difference between the bottom and top wall is increased above a threshold value.

When the Reynolds number exceeds the critical value of 5,400, 2-D Tollmien-Schlichting (T-S) waves are amplified. In accordance with Gage and Reid,  $^{10}$  for  $Re > Re_c = 5,400$  and  $Ra < Ra_c = 1,708$ , 2-D transverse waves (T-S waves) which are aligned perpendicular to the flow direction are unstable. Numerous scientific papers have been published on the stability of laminar zero-pressure gradient boundary layers for which T-S waves are the primary instability mode.  $^{23-26}$  But research on the viscosity-driven instability of channel flows is very sparse. Orszag<sup>27</sup> obtained solutions of the Orr-Sommerfeld equation for the stability analysis of plane Poiseuille flow and found that the critical Reynolds number for which the flow becomes unstable is 5,772.22. The stability of plane Poiseuille flow was examined experimentally by Nishioka et al.  $^{28}$  The downstream development of sinusoidal waves at Reynolds numbers ranging from 3,000 to 7,500 was scrutinized. The measurements were in accordance with linear stability theory as long as the disturbances were small. A nonlinear sub-critical (Reynolds number below critical Reynolds number for linear stability) instability was discovered when the disturbance level exceeded a certain threshold value. Lee et al.  $^{29}$  investigated the effect of wall-normal blowing and suction on the stability of a laminar channel flow based on Floquet analysis and direct numerical simulations. Their analysis revealed that the traveling waves

resulting from wall-normal blowing and suction were amplified when the phase speed was approximately 0.4 times the maximum (centerline) velocity and Tollmien-Schlichting waves were observed for Re = 2,000 and Re = 7,500. A similar investigation of the spatial stability of plane Poiseuille flow for two different Reynolds numbers (5,000 & 10,000) was carried out by Chung et al.<sup>30</sup> Overall, apart from the Gage and Reid<sup>10</sup> paper, the published literature on the instability of plane Poiseuille flow with vertical temperature gradient is very limited.

This paper reports on temporal stability simulations that were carried out to investigate both the buoyancy and viscosity-driven instability of plane Rayleigh-Bénard-Poiseuille flow. Two highly accurate computational fluid dynamics codes based on the compressible Navier-Stokes equations were developed especially for this purpose. The details of these codes are discussed first. Different 2-D and 3-D cases were simulated and the wavelengths, growth rates, phase speeds, frequencies, amplitudes and phase distributions of the disturbance modes were analyzed using Fourier transforms. The growth rates obtained from the temporal stability simulations are compared with the Gage and Reid<sup>10</sup> neutral curves. This paper makes a contribution to the existing literature by providing mode amplitude and phase distributions as well as dispersion relationships for RBP flow. In addition, the paper provides new physical insight into non-linear mode interactions.

#### II. Methodology

## **Full Navier-Stokes Equations**

The compressible Navier-Stokes equations in conservative form can be written as a vector equation,

$$\frac{\partial \mathbf{Q}}{\partial t} + \frac{\partial \mathbf{E}}{\partial x} + \frac{\partial \mathbf{F}}{\partial y} + \frac{\partial \mathbf{G}}{\partial z} = \mathbf{H}, \qquad (3)$$

with state vector,

$$\mathbf{Q} = \begin{bmatrix} \rho \\ \rho u \\ \rho v \\ \rho w \\ \rho e \end{bmatrix}, \tag{4}$$

and flux vectors,

$$\mathbf{E} = \begin{bmatrix} \rho u \\ \rho u^{2} + p - \tau_{xx} \\ \rho uv - \tau_{xy} \\ \rho uw - \tau_{xz} \\ u(\rho e + p) - u\tau_{xx} - v\tau_{xy} - w\tau_{xz} + q_{x} \end{bmatrix},$$

$$\mathbf{F} = \begin{bmatrix} \rho v \\ \rho vu - \tau_{xy} \\ \rho vv - \tau_{yz} \\ v(\rho e + p) - u\tau_{xy} - v\tau_{yy} - w\tau_{yz} + q_{y} \end{bmatrix},$$

$$(5)$$

$$\mathbf{F} = \begin{bmatrix} \rho v \\ \rho v u - \tau_{xy} \\ \rho v^2 + p - \tau_{yy} \\ \rho v w - \tau_{yz} \\ v(\rho e + p) - u \tau_{xy} - v \tau_{yy} - w \tau_{yz} + q_y \end{bmatrix},$$
(6)

and

$$\mathbf{G} = \begin{bmatrix} \rho w \\ \rho w u - \tau_{xz} \\ \rho w v - \tau_{yz} \\ \rho w^2 + p - \tau_{zz} \\ w(\rho e + p) - u \tau_{xz} - v \tau_{yz} - w \tau_{zz} + q_z \end{bmatrix} . \tag{7}$$

Here, u, v, and w are the velocities in the streamwise, wall-normal, and spanwise direction,  $\rho$  is the density, p is the static pressure, and T is the temperature. The total energy is  $e = \epsilon + 1/2(u^2 + v^2 + w^2)$ , where  $\epsilon = c_v T$  is the internal energy. The source term vector,

$$\mathbf{H} = \begin{bmatrix} 0 \\ \frac{\partial p}{\partial x} \\ g(\rho_{ref} - \rho) \\ 0 \\ u\frac{\partial p}{\partial x} + vg(\rho_{ref} - \rho) \end{bmatrix}, \tag{8}$$

contains a  $\partial p/\partial x$  term that compensates for the streamwise pressure drop resulting from the viscous losses, and a buoyancy term,  $g(\rho_{ref}-\rho)$  (Boussinesq approximation), with gravitational acceleration,  $g=9.81m/s^2$ . The shear stress tensor components are,

$$\tau_{xx} = \mu \frac{2}{3} \left( 2 \frac{\partial u}{\partial x} - \frac{\partial v}{\partial y} - \frac{\partial w}{\partial z} \right) \tag{9}$$

$$\tau_{yy} = \mu \frac{2}{3} \left( 2 \frac{\partial v}{\partial y} - \frac{\partial u}{\partial x} - \frac{\partial w}{\partial z} \right) \tag{10}$$

$$\tau_{zz} = \mu \frac{2}{3} \left( 2 \frac{\partial w}{\partial z} - \frac{\partial u}{\partial x} - \frac{\partial v}{\partial y} \right) \tag{11}$$

$$\tau_{xy} = \mu \left( \frac{\partial u}{\partial y} + \frac{\partial v}{\partial x} \right) \tag{12}$$

$$\tau_{xz} = \mu \left( \frac{\partial u}{\partial z} + \frac{\partial w}{\partial x} \right) \tag{13}$$

$$\tau_{yz} = \mu \left( \frac{\partial v}{\partial z} + \frac{\partial w}{\partial y} \right), \tag{14}$$

with dynamic viscosity,  $\mu$ . The heat flux vector components are,

$$q_x = -k\frac{\partial T}{\partial x} \tag{15}$$

$$q_y = -k \frac{\partial T}{\partial y} \tag{16}$$

$$q_z = -k \frac{\partial T}{\partial z}, \tag{17}$$

with thermal conductivity,

$$k = \frac{c_p}{P_r}\mu. (18)$$

Here, Pr and  $c_p$  are the Prandtl number and specific heat. The Prandtl number is defined as

$$Pr = \frac{\nu}{\alpha} \,. \tag{19}$$

where  $\nu = \mu/\rho$  is the kinematic viscosity and  $\alpha$  is the thermal diffusivity. The set of equations is closed by the ideal gas equation,

$$p = \rho RT, \tag{20}$$

with gas constant, R, and Sutherland's equation for the dynamic viscosity,  $\mu$ .

## Linearized Navier-Stokes Equations

A disturbance ansatz is made for the linearization. All flow quantities are split up into a base flow (mean) and disturbance component,

$$\rho = \bar{\rho} + \rho' \tag{21}$$

$$u = \bar{u} + u' \tag{22}$$

$$v = \bar{v} + v' \tag{23}$$

$$w = \bar{w} + w' \tag{24}$$

$$T = \bar{T} + T' \tag{25}$$

$$p = \bar{p} + p' \tag{26}$$

$$\mu = \bar{\mu} + \mu' \,. \tag{27}$$

The linearized compressible Navier-Stokes equations in conservative form can be written in vector form,

$$\frac{\partial \mathbf{Q}'}{\partial t} + \frac{\partial \mathbf{E}'}{\partial x} + \frac{\partial \mathbf{F}'}{\partial y} + \frac{\partial \mathbf{G}'}{\partial z} = \mathbf{H}', \qquad (28)$$

with disturbance state vector,

$$\mathbf{Q}' = \begin{bmatrix} \rho' \\ \bar{\rho}u' + \rho'\bar{u} \\ \bar{\rho}v' + \rho'\bar{v} \\ \bar{\rho}w' + \rho'\bar{w} \\ \bar{\rho}e' + \rho'\bar{e} \end{bmatrix}, \tag{29}$$

and flux vectors,

$$\mathbf{E}' = \begin{bmatrix} \bar{\rho}u' + \rho'\bar{u} \\ 2(\bar{\rho}\bar{u})u' + \rho'\bar{u}^2 + p' - \tau'_{xx} \\ (\bar{\rho}\bar{u})v' + \bar{v}(\bar{\rho}u' + \rho'\bar{u}) - \tau'_{xy} \\ (\bar{\rho}\bar{u})w' + \bar{w}(\bar{\rho}u' + \rho'\bar{u}) - \tau'_{xz} \\ (\bar{\rho}\bar{u})w' + \bar{w}(\bar{\rho}u' + \rho'\bar{u}) - \tau'_{xz} \\ (\bar{\rho}\bar{e})u' + \bar{u}(\bar{\rho}e' + \rho'\bar{e}) + (\bar{p}u' + p'\bar{u}) - (\bar{u}\tau'_{xx} + u'\bar{\tau}_{xx}) - (\bar{v}\tau'_{xy} + v'\bar{\tau}_{xy}) - (\bar{w}\tau'_{xz} + w'\bar{\tau}_{xz}) + q'_{x} \end{bmatrix},$$

$$\mathbf{F}' = \begin{bmatrix} \bar{\rho}v' + \rho'\bar{v} \\ (\bar{\rho}\bar{v})u' + \bar{u}(\bar{\rho}v' + \rho'\bar{v}) - \tau'_{xy} \\ (2(\bar{\rho}\bar{v})v' + \rho'\bar{v}^2 + p' - \tau'_{yy} \\ (\bar{\rho}\bar{v})w' + \bar{w}(\bar{\rho}v' + \rho'\bar{v}) - \tau'_{yz} \\ (\bar{\rho}\bar{e})v' + \bar{v}(\bar{\rho}e' + \rho'\bar{e}) + (\bar{p}v' + p'\bar{v}) - (\bar{u}\tau'_{xy} + u'\bar{\tau}_{xy}) - (\bar{v}\tau'_{yy} + v'\bar{\tau}_{yy}) - (\bar{w}\tau'_{yz} + w'\bar{\tau}_{yz}) + q'_{y} \end{bmatrix},$$

$$(31)$$

$$\mathbf{F}' = \begin{bmatrix} \bar{\rho}v' + \rho'\bar{v} \\ (\bar{\rho}\bar{v})u' + \bar{u}(\bar{\rho}v' + \rho'\bar{v}) - \tau'_{xy} \\ 2(\bar{\rho}\bar{v})v' + \rho'\bar{v}^2 + p' - \tau'_{yy} \\ (\bar{\rho}\bar{v})w' + \bar{w}(\bar{\rho}v' + \rho'\bar{v}) - \tau'_{yz} \\ (\bar{\rho}\bar{e})v' + \bar{v}(\bar{\rho}e' + \rho'\bar{e}) + (\bar{p}v' + p'\bar{v}) - (\bar{u}\tau'_{xy} + u'\bar{\tau}_{xy}) - (\bar{v}\tau'_{yy} + v'\bar{\tau}_{yy}) - (\bar{w}\tau'_{yz} + w'\bar{\tau}_{yz}) + q'_{y} \end{bmatrix},$$
(31)

$$\mathbf{G}' = \begin{bmatrix} \bar{\rho}w' + \rho'\bar{w} \\ (\bar{\rho}\bar{w})u' + \bar{u}(\bar{\rho}w' + \rho'\bar{w}) - \tau'_{xz} \\ (\bar{\rho}\bar{w})v' + \bar{v}(\bar{\rho}w' + \rho'\bar{w}) - \tau'_{yz} \\ (\bar{\rho}\bar{w})w' + \rho'\bar{w}^2 + p' - \tau'_{zz} \\ (\bar{\rho}\bar{e})w' + \bar{w}(\bar{\rho}e' + \rho'\bar{e}) + (\bar{p}w' + p'\bar{w}) - (\bar{u}\tau'_{xz} + u'\bar{\tau}_{xz}) - (\bar{v}\tau'_{yz} + v'\bar{\tau}_{yz}) - (\bar{w}\tau'_{zz} + w'\bar{\tau}_{zz}) + q'_z \end{bmatrix}.$$
(32)

The disturbance total energy is  $e' = \epsilon' + \bar{u}u' + \bar{v}v' + \bar{w}w'$ , where  $\epsilon' = c_v T'$  is the internal energy. The source term vector is

$$\mathbf{H}' = \begin{bmatrix} 0 \\ 0 \\ -g\rho' \\ 0 \\ u'\frac{\partial\bar{p}}{\partial x} + v'g(1-\bar{\rho}) - \bar{v}g\rho' \end{bmatrix}. \tag{33}$$

The shear stress tensor components are,

$$\tau'_{xx} = \bar{\mu} \frac{2}{3} \left( 2 \frac{\partial u'}{\partial x} - \frac{\partial v'}{\partial y} - \frac{\partial w'}{\partial z} \right) + \mu' \frac{2}{3} \left( 2 \frac{\partial \bar{u}}{\partial x} - \frac{\partial \bar{v}}{\partial y} - \frac{\partial \bar{w}}{\partial z} \right)$$
(34)

$$\tau_{yy}' = \bar{\mu} \frac{2}{3} \left( 2 \frac{\partial v'}{\partial y} - \frac{\partial u'}{\partial x} - \frac{\partial w'}{\partial z} \right) + \mu' \frac{2}{3} \left( 2 \frac{\partial \bar{v}}{\partial y} - \frac{\partial \bar{u}}{\partial x} - \frac{\partial \bar{w}}{\partial z} \right) \tag{35}$$

$$\tau'_{zz} = \bar{\mu} \frac{2}{3} \left( 2 \frac{\partial w'}{\partial z} - \frac{\partial u'}{\partial x} - \frac{\partial v'}{\partial y} \right) + \mu' \frac{2}{3} \left( 2 \frac{\partial \bar{w}}{\partial z} - \frac{\partial \bar{u}}{\partial x} - \frac{\partial \bar{v}}{\partial y} \right)$$
(36)

$$\tau'_{xy} = \bar{\mu} \left( \frac{\partial u'}{\partial y} + \frac{\partial v'}{\partial x} \right) + \mu' \left( \frac{\partial \bar{u}}{\partial y} + \frac{\partial \bar{v}}{\partial x} \right)$$
 (37)

$$\tau'_{xz} = \bar{\mu} \left( \frac{\partial u'}{\partial z} + \frac{\partial w'}{\partial x} \right) + \mu' \left( \frac{\partial \bar{u}}{\partial z} + \frac{\partial \bar{w}}{\partial x} \right)$$
(38)

$$\tau'_{yz} = \bar{\mu} \left( \frac{\partial v'}{\partial z} + \frac{\partial w'}{\partial y} \right) + \mu' \left( \frac{\partial \bar{v}}{\partial z} + \frac{\partial \bar{w}}{\partial y} \right), \tag{39}$$

and the heat flux vector components are,

$$q_x' = -\left(\bar{k}\frac{\partial T'}{\partial x} + k'\frac{\partial \bar{T}}{\partial x}\right) \tag{40}$$

$$q_y' = -\left(\bar{k}\frac{\partial T'}{\partial y} + k'\frac{\partial \bar{T}}{\partial y}\right) \tag{41}$$

$$q_z' = -\left(\bar{k}\frac{\partial T'}{\partial z} + k'\frac{\partial \bar{T}}{\partial z}\right). \tag{42}$$

The disturbance component of the dynamic viscosity and heat conductivity are

$$\mu' = \frac{\partial \bar{\mu}}{\partial \bar{T}} T' \tag{43}$$

and

$$k' = \frac{\partial \bar{k}}{\partial \bar{T}} T' = \frac{c_p}{Pr} \frac{\partial \bar{\mu}}{\partial \bar{T}} T'. \tag{44}$$

The disturbance pressure is

$$p' = R(\rho'\bar{T} + \bar{\rho}T'). \tag{45}$$

#### C. Base Flow

The base or basic flow for the simulations was obtained by solving the one-dimensional (1-D) Navier-Stokes equations. The equations governing 1-D laminar plane RBP flow are,

$$\frac{\partial p}{\partial x} = \mu \frac{\partial^2 u}{\partial y^2} \,, \tag{46}$$

$$\frac{\partial p}{\partial y} = (1 - \rho)g\,,\tag{47}$$

$$k\frac{\partial^2 T}{\partial u^2} + \mu \left(\frac{\partial u}{\partial u}\right)^2 = 0. \tag{48}$$

The equations were derived from the incompressible Navier-Stokes equations under the assumption of parallel flow  $(\partial/\partial x = 0)$ , where x is the streamwise coordinate), zero wall-normal velocity (v = 0), and steady flow  $(\partial/\partial t = 0)$ .

## D. Channel Flow Relationships

The hydraulic diameter for a 2-D channel flow (height h and span b) is defined as

$$D_h = \frac{4b \times h}{2(b+h)} \,. \tag{49}$$

For a channel with infinite width or span  $(b \to \infty)$ ,  $D_h = 2h$ . The bulk velocity is defined as

$$u_b = \frac{1}{h} \int u \, dy \,. \tag{50}$$

From the x-momentum equation for a constant temperature laminar 2-D channel flow,

$$\nu \frac{\partial^2 u}{\partial y^2} = \frac{1}{\rho} \frac{\partial p}{\partial x},\tag{51}$$

the velocity profile can be found by integration

$$u = \frac{1}{2\rho\nu} \frac{\partial p}{\partial x} \left( y^2 - hy \right) . \tag{52}$$

The maximum velocity is obtained at the channel half-height,

$$u_{max} = -\frac{h^2}{8\rho\nu} \frac{\partial p}{\partial x} \,. \tag{53}$$

The velocity profile expressed in terms of the maximum velocity is

$$u = 4u_{max} \left[ \frac{y}{h} - \left( \frac{y}{h} \right)^2 \right] . \tag{54}$$

From this the bulk velocity for the laminar profile can be obtained.

$$u_b = \frac{2}{3}u_{max} \,. \tag{55}$$

The skin-friction coefficient can be computed from the near-wall gradient of the velocity profile,

$$\frac{\partial u}{\partial y} = 4u_{max} \left( \frac{1}{h} - 2\frac{y}{h^2} \right) . \tag{56}$$

At the wall,

$$\frac{\partial u}{\partial y} = 4 \frac{u_{max}}{h} \,, \tag{57}$$

and the skin-friction coefficient based on the bulk velocity becomes,

$$c_f = \frac{\rho \nu \frac{\partial u}{\partial y}}{\frac{1}{2}\rho u_b^2} = 12 \frac{\nu}{u_b h} \,. \tag{58}$$

The Darcy friction factor, f, is defined as

$$\frac{\partial p}{\partial x} = -\frac{1}{2}\rho u_b^2 \frac{f}{D_b} \,. \tag{59}$$

From a control volume analysis in the streamwise direction for a channel with span b,

$$hb\frac{\partial p}{\partial x}dx + \tau 2bdx = 0, (60)$$

the skin friction can be acquired,

$$\tau = -\frac{h}{2} \frac{\partial p}{\partial x} \,. \tag{61}$$

Making use of the friction factor,

$$\tau = \frac{h}{2} \frac{1}{2} \rho u_b^2 \frac{f}{D_b} = \frac{f}{8} \rho u_b^2 \,, \tag{62}$$

is obtained which is valid for both laminar and turbulent channel flow. With this the skin-friction coefficient becomes

$$c_f = \frac{\tau}{\frac{1}{2}\rho u_b^2} = \frac{f}{4} \,. \tag{63}$$

#### E. Non-Dimensionalization

The governing equations were made dimensionless with a reference velocity,  $v_{ref}$ , a reference length scale,  $L_{ref}$ , a reference temperature,  $T_{ref}$ , and a reference density,  $\rho_{ref}$ . Pressure was non-dimensionalized with  $\rho_{ref}v_{ref}^2$ . The Reynolds number based on bulk velocity and hydraulic diameter is

$$Re_b = \frac{u_b 2h}{\nu} \,, \tag{64}$$

where h is the channel height. Gage and Reid<sup>10</sup> based their Reynolds number on the maximum velocity and channel half height,

$$Re = \frac{u_{max}\frac{h}{2}}{\nu} \,. \tag{65}$$

Using the expression for the bulk velocity,

$$Re_b \approx \frac{4}{3} \frac{u_{max}h}{\nu} = \frac{8}{3} Re \,, \tag{66}$$

is obtained where the approximate sign indicates that the expression is only valid for constant temperature flow. For the present simulations, the bulk velocity was taken as reference velocity,  $v_{ref} = u_b$ , and the channel half-height was taken as reference length,  $L_{ref} = h/2$ . The resulting reference Reynolds number is

$$Re_{ref} = \frac{v_{ref}L_{ref}}{\nu} = \frac{u_b \frac{h}{2}}{\nu} = \frac{1}{4}Re_b \approx \frac{2}{3}Re,$$
 (67)

For laminar flow  $c_f = 24/Re_b$  and therefore  $f = 96/Re_b = 24/Re_{ref}$ . The negative pressure gradient made dimensionless with the reference length,  $L_{ref} = h/2$ , and the bulk velocity,  $u_b$  is

$$-\frac{\partial p}{\partial x}\frac{\frac{h}{2}}{\rho u_b^2} = \frac{f}{8} = \frac{dp}{dx}.$$
 (68)

For the present simulations, this expression is added as a source term to the right-hand-side of the streamwise momentum equation to maintain a constant bulk velocity.

The Rayleigh number is defined as

$$Ra = \frac{\gamma h^3 g \Delta T}{\nu \alpha} \,, \tag{69}$$

where  $\gamma = 1/T_{av}$  with  $T_{av} = (T_{hot} + T_{cold})/2$  is the thermal expansion coefficient for a perfect gas, and  $\Delta T = T_{hot} - T_{cold}$ , is the temperature difference between the bottom and top wall. The Rayleigh number can be written as

$$Ra = Re_{ref}^2 \frac{\Delta T}{T_{av}} \left(\frac{h}{L_{ref}}\right)^3 \left(g \frac{L_{ref}}{v_{ref}^2}\right) Pr, \qquad (70)$$

where  $gL_{ref}/v_{ref}^2$  is the dimensionless gravitational acceleration. In accordance with Gage and Reid<sup>10</sup> the Prandtl number was set to one. The reference Mach number for the present simulations was 0.1.

#### F. Discretization

A grid transformation was employed for the convective terms of the Navier-Stokes equations in the wall-normal direction. The resulting first derivatives were discretized with fifth-order-accurate upwind-biased,

$$\frac{1}{2}f'_{j-1} + f'_j + \frac{1}{6}f'_{j+1} = -\frac{1}{18}f_{j-2} - f_{j-1} + \frac{1}{2}f_j + \frac{5}{9}f_{j+1},$$
 (71)

and downwind-biased,

$$\frac{1}{2}f'_{j+1} + f'_{j} + \frac{1}{6}f'_{j-1} = \frac{1}{18}f_{j+2} + f_{j+1} - \frac{1}{2}f_{j} - \frac{5}{9}f_{j-1},$$
 (72)

	d = 1	d = 2
$a_{j-1}$	$\{\frac{h_{j+1}}{h_{j+1}+h_j}\}^2$	$\left\{\frac{h_{j+1}}{h_j + h_{j+1}}\right\} \left\{\frac{h_j^2 + h_j h_{j+1} - h_{j+1}^2}{h_j^2 + 3h_j h_{j+1} + h_{j+1}^2}\right\}$
$a_{j+1}$	$\{\frac{h_j}{h_{j+1} + h_j}\}^2$	$\left\{\frac{h_j}{h_j + h_{j+1}}\right\} \left\{\frac{h_{j+1}^2 + h_j h_{j+1} - h_j^2}{h_j^2 + 3h_j h_{j+1} + h_{j+1}^2}\right\}$
$b_{j-1}$	$-\frac{2h_{j+1}^2\{2h_j+h_{j+1}\}}{h_j\{h_{j+1}+h_j\}^3}$	$\left\{\frac{h_{j+1}}{h_j + h_{j+1}}\right\} \left\{\frac{12}{h_j^2 + 3h_j h_{j+1} + h_{j+1}^2}\right\}$
$b_j$	$rac{2\{h_{j+1}-h_{j}\}}{h_{j}h_{j+1}}$	$\frac{-12}{h_j^2 + 3h_j h_{j+1} + h_{j+1}^2}$
$b_{j+1}$	$\frac{2h_j^2\{h_j+2h_{j+1}\}}{h_{j+1}\{h_{j+1}+h_j\}^3}$	$\left\{\frac{h_j}{h_j + h_{j+1}}\right\} \left\{\frac{12}{h_j^2 + 3h_j h_{j+1} + h_{j+1}^2}\right\}$

Table 1. Coefficients for fourth-order accurate compact finite difference stencils for non-uniform grids.<sup>32</sup>

compact finite differences.<sup>31</sup> For the spatial discretization of the 1st and 2nd derivatives that appear in the viscous terms, fourth-order-accurate compact finite differences for non-equidistant meshes by Shukla et al.<sup>32</sup> were utilized in the wall-normal direction,

$$a_{j-1}f_{j-1}^{(d)} + f_j^{(d)} + a_{j+1}f_{j+1}^{(d)} = b_{j-1}f_{j-1} + b_jf_j + b_{j+1}f_{j+1}.$$
 (73)

Here d (either 1 or 2) represents the order of the derivative. The coefficients are provided in Tab. 1 where  $h_j = y_j - y_{j-1}$  corresponds to the wall-normal grid spacing. The resulting tridiagonal systems of equations were solved with the Thomas algorithm. Streamwise (x-coordinate) and spanwise (z-coordinate) derivatives were calculated in Fourier space.<sup>2,18</sup> The forward and backward Fourier transforms were computed with fast Fourier transforms (FFTs).<sup>33,34</sup>

A fourth-order-accurate Runge-Kutta method $^{35}$  was applied for advancing the governing equations in time,

$$\mathbf{Q}_1 = \mathbf{Q}^n + \frac{\Delta t}{2} \mathbf{R}(\mathbf{Q}^n) \tag{74}$$

$$\mathbf{Q}_2 = \mathbf{Q}^n + \frac{\Delta t}{2} \mathbf{R}(\mathbf{Q}_1)$$

$$\mathbf{Q}_1 \quad \Leftarrow \quad \mathbf{Q}_1 + 2\mathbf{Q}_2 \tag{75}$$

$$\mathbf{Q}_2 = \mathbf{Q}^n + \Delta t \mathbf{R}(\mathbf{Q}_2)$$

$$\mathbf{Q}_1 \quad \Leftarrow \quad \frac{1}{2}(-\mathbf{Q}^n + \mathbf{Q}_1 + \mathbf{Q}_2) \tag{76}$$

$$\mathbf{Q}^{n+1} = \mathbf{Q}_1 + \frac{\Delta t}{6} \mathbf{R}(\mathbf{Q}_2), \qquad (77)$$

where n and n+1 are the old and new time step and

$$\frac{\partial \mathbf{Q}}{\partial t} = \mathbf{R} = \mathbf{H} - \frac{\partial \mathbf{E}}{\partial x} - \frac{\partial \mathbf{F}}{\partial y} - \frac{\partial \mathbf{G}}{\partial z}.$$
 (78)

## G. Computational Domain

A coordinate transformation was employed in the wall-normal direction (grid line index, j; coordinate in computational space,  $\eta = j$ ;  $\Delta \eta = 1$ ) that clusters grid points near the walls. A total of J grid points were distributed in the wall-normal direction,

$$y_j = \left[ \frac{\tan^{-1}(jc - f_1)}{f_2} + 1 \right] \times \frac{h}{2}, \tag{79}$$

where h is the channel height, c is a user specified constant,  $f_1 = Jc/2$ , and  $f_2 = \tan^{-1}(f_1)$ . The derivative of the computational coordinate with respect to the physical coordinate is,

$$\frac{\partial \eta}{\partial y} = 2\frac{f_2}{ch} \left\{ 1 + \tan^2 \left[ \left( \frac{2y}{h} - 1 \right) f_2 \right] \right\}, \tag{80}$$

and the derivative in physical space can be obtained from

$$\frac{\partial f}{\partial y} = f' \frac{\partial \eta}{\partial y} \,. \tag{81}$$

## H. Boundary Conditions

For the full Navier-Stokes (FNS) simulations, no-slip and no-penetration boundary conditions were enforced at the walls. The bottom and top wall temperature were held constant at 350K and 300K, respectively. Assuming  $\partial \rho v/\partial t = 0$  and  $\partial/\partial x = 0$  at the wall, the momentum equation in the y-direction at the wall simplifies to

$$\frac{\partial p}{\partial y} = g(1 - \rho). \tag{82}$$

When the pressure differential is discretized with a one-sided fourth-order-accurate finite difference stencil, the wall pressure at the bottom and top wall become,

$$p_0 = \frac{-12g\frac{\partial y}{\partial \eta} + 48p_1 - 36p_2 + 16p_3 - 3p_4}{25 - \frac{12g}{RT_0}\frac{\partial y}{\partial \eta}},$$
(83)

and

$$p_{jx} = \frac{12g\frac{\partial y}{\partial \eta} + 48p_{jx-1} - 36p_{jx-2} + 16p_{jx-3} - 3p_{jx-4}}{25 + \frac{12g}{RT_{ix}}\frac{\partial y}{\partial \eta}}.$$
 (84)

For the linearized Navier-Stokes (LNS) simulations, the streamwise, wall-normal and spanwise disturbance velocity, u', v' and w', as well as the disturbance temperature, T', were set to zero at both the top and bottom wall. The linearized wall-normal momentum equation at the wall simplifies to

$$\frac{\partial p'}{\partial u} = -g\rho' \,. \tag{85}$$

By making use of T'=0 in Eq. 45, an expression for the disturbance density at the wall is obtained,

$$\rho' = \frac{p'}{R\bar{T}} \,, \tag{86}$$

Using one-sided fourth-order-accurate standard finite difference stencils, the disturbance wall pressure at the bottom and top wall can be found,

$$p_0' = \frac{48p_1' - 36p_2' + 16p_3' - 3p_4'}{25 - \frac{12g}{RT_0} \frac{\partial y}{\partial \eta}},$$
(87)

and

$$p'_{jx} = \frac{48p'_{jx-1} - 36p'_{jx-2} + 16p'_{jx-3} - 3p_{jx-4}}{25 + \frac{12g}{RT_{jx}} \frac{\partial y}{\partial \eta}}.$$
 (88)

#### I. Numerical Linear Stability Analysis

According to what is customary in linear stability theory (LST), a wave ansatz of the form

$$v'(x, y, z, t) = \sum \hat{v}(y)e^{i(\alpha x + \beta z - \omega t)}, \qquad (89)$$

is made for the disturbances where  $\alpha = \alpha_r + i\alpha_i$ ,  $\beta$  and  $\omega = \omega_r + i\omega_i$  are the streamwise wavenumber, spanwise wavenumber and angular frequency, respectively. Here,  $\hat{v}(y)$  are the eigenfunctions. The streamwise,  $\lambda_x$ , and spanwise,  $\lambda_z$ , wavelengths can be obtained from the streamwise and spanwise wavenumbers,  $\alpha_r = 2\pi/\lambda_x$  and  $\beta = 2\pi/\lambda_z$ . The wavelengths  $\lambda_x$  and  $\lambda_z$  are related to the streamwise domain extent, L, and the spanwise domain extent, L, through L and L are the streamwise and spanwise mode number. The period, L is related to the real part of the angular frequency via L and L are the streamwise and spanwise mode number.

For the temporal stability simulations discussed in this paper, the disturbances can only grow or decay in time and therefore,  $\alpha_i = 0$ . The disturbances can then be expressed as,

$$v'(x, y, z, t) = \sum \hat{v}(y)e^{i[\alpha_r x + \beta z - (\omega_r + i\omega_i)t]}$$

$$= \sum \hat{v}(y)e^{i(\alpha_r x + \beta z - \omega_r t)}e^{\omega_i t}$$

$$= \sum e^{i\psi}A[v'(y, t)], \qquad (90)$$

where the sum is taken over all Fourier modes and A and  $\psi = \alpha_r x + \beta z - \omega_r t$  are the Fourier mode amplitude and phase. Accordingly, the temporal growth rates of the modes can be computed from

$$\omega_i = \frac{\partial \ln A(v')}{\partial t} \,, \tag{91}$$

and the phase speed can be computed from

$$c = \frac{\omega_r}{\alpha_r} = -\frac{\frac{\partial \psi}{\partial x}}{\frac{\partial \psi}{\partial t}}.$$
 (92)

The wave angle is defined as  $\lambda = tan^{-1}(\beta/\alpha)$ .

#### III. Validation

The temporal stability of plane Poiseuille flow (no heated walls, no gravitational field) is considered first to validate the present numerical simulations. Several researchers investigated the onset of hydrodynamic instability in plane Poiseuille flow numerically. The first numerical solutions of the Orr-Sommerfeld stability equation were obtained by Thomas is give-point Numerov finite difference method. Using 50 and 100 grid points, Thomas found phase speeds of c=0.2375006+0.0035925i and c=0.2375243+0.0037312i, respectively, for  $\alpha_r=1$  and Re=10,000. Gary and Helgason meloyed a sixth-order-accurate finite difference scheme for stretched coordinates and obtained c=0.23752964+0.00374248i (43 grid points) and c=0.23752650+0.00373969i (100 grid points) for the same case. An accurate solution of the Orr-Sommerfeld stability equation was achieved by Orszag<sup>27</sup> using Chebyshev polynomials. According to Orszag, the correct phase speed for  $\alpha_r=1$  and Re=10,000 is c=0.23752679+0.00373967i.

J	$c = c_r + ic_i$	$ \text{Error}(\%)  \text{ for } c_i$
48	$0.234799755 {+} 0.008879324 \mathrm{i}$	137.43
72	$0.235279754 \!+\! 0.004574262 \mathrm{i}$	22.31
96	$0.236793086 {+} 0.003758063 \mathrm{i}$	0.49
120	$0.237386419 \! + \! 0.003677396\mathrm{i}$	1.66
144	$0.237606418 \! + \! 0.003677863 \mathrm{i}$	1.65
168	$0.237693085 \!+\! 0.003683529 \mathrm{i}$	1.50
192	$0.237733085 \!+\! 0.003686796 \mathrm{i}$	1.41
216	$0.237759752 \!+\! 0.003689329 \mathrm{i}$	1.34
240	0.237766418 + 0.003691996i	1.27
264	0.237779752 + 0.003691396i	1.29
288	0.237779752 + 0.003692396i	1.26
312	0.237779752 + 0.003692663i	1.25

Table 2. Phase speed vs. wall-normal grid resolution and relative error with respect to Orszag<sup>27</sup> result.

The base flow for the LNS validation simulations of the  $Orszag^{27}$  case was computed as explained in section II.C. The top and bottom wall temperature were set to 300K which results in Ra=0. A number of LNS simulations with different wall-normal grid resolutions were carried out and the phase speed error was calculated with respect to the reference value obtained by  $Orszag^{27}$  (Tab. 2). As the grid resolution was

increased, the phase speed obtained from the present simulations converged to the phase speed published in the literature.<sup>27</sup> The small remaining residue error can be explained by the fact that Orszag<sup>27</sup> solved the incompressible Navier-Stokes equations.

#### IV. Results

Numerical analyses for different stable and unstable cases in the vicinity of the stability boundaries provided by Gage and Reid<sup>10</sup> (Fig. 1 and Tab. 3) were performed. The number of Fourier modes in the streamwise and spanwise direction counted from 0 is lmax and kmax, respectively. The individual cases are either (1) stable ( $Re < Re_c \& Ra < Ra_c$ ), (2) unstable with respect to 3-D waves (buoyancy-driven instability,  $Re < Re_c \& Ra > Ra_c$ ), and (3) unstable with respect to 2-D waves (viscosity-driven instability,  $Re > Re_c \& Ra < Ra_c$ ). For all simulations, very small (linear) disturbances were added to the initial condition to raise the disturbance amplitudes slightly above machine roundoff. For parallel channel flow, the wall-normal velocity is zero. The disturbance amplitudes, growth rates, frequencies, and phase speeds were computed from the wall-normal velocity component in the center of the channel.

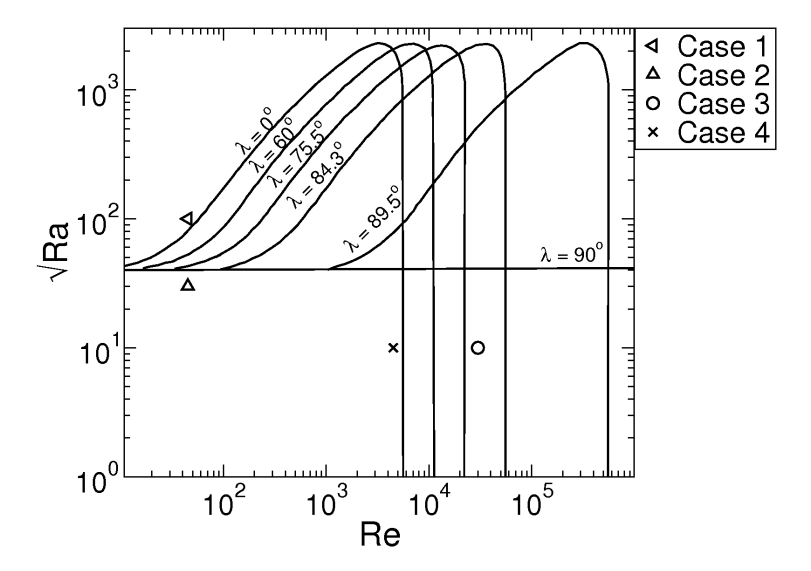


Figure 1. Neutral curves from stability analyses by Gage and  ${\rm Reid.^{10}}$  Symbols represent parameters for present simulations.

	Dimensions	L	Z	lmax	kmax	Re	$\sqrt{Ra}$	Type of instability
Case 1	3-D	-	12	1	16	44.984	100	Buoyancy-driven
Case 2	3-D	-	12	1	8	45.010	30	Buoyancy-driven
Case 3	2-D	30	-	16	1	30008.037	10	Viscosity-driven
Case 4	2-D	22.5	-	4	1	4501.626	10	Viscosity-driven

Table 3. Parameters for 2-D and 3-D simulations.

## A. Buoyancy Driven Instability

A grid resolution study was conducted for Re = 44.984 and  $\sqrt{R}a = 100$  before proceeding further. Several linearized simulations were carried out using only two spanwise Fourier modes (k = 0 and k = 1). The spanwise grid extent was held constant at Z = 3 ( $\lambda_z = 3$  and  $\beta = 2.094$ ) and the number of grid points, J, in the wall-normal direction was varied. Based on the data provided in Tab. 4, it was decided to use J = 72 for all simulations with buoyancy-driven instability. The Reynolds number, Rayleigh number, and

spanwise domain extent for case 1 are Re=44.984,  $\sqrt{R}a=100$  and Z=12 (Tab. 3). According to Gage and Reid,  $^{10}$  case 1 is unstable. To determine how the wavelength, growth rate and amplitude of the unstable mode depends on the spanwise wavenumber, the spanwise domain extent, Z, was varied. The growth rates obtained from the LNS simulations are listed in Tab. 5 and plotted versus the spanwise wavenumber in Fig. 2. The highest growth rate ( $\omega_i=0.2181$ ) is obtained for a spanwise wavenumber of  $\beta=2.094$  which corresponds to a spanwise wavelength of  $\lambda_z=2\pi/\beta=3$ . The growth rate becomes zero for  $\beta\approx0.417$  and  $\beta\approx4.178$ . The very low and very high wavenumbers would of course be difficult to observe in practice since the  $\beta=2.094$  disturbances grow much faster and develop first into observable flow structures.

J	$\omega_i$
48	0.218147
60	0.218141
72	0.218134
84	0.218134
96	0.218127

Table 4. Grid resolution study for Re=44.984 and  $\sqrt{Ra}=100$  (case 1).

$\lambda_z$	β	$\omega_i$
1.25	5.026	-0.1775
1.5	4.188	-0.0010
2	3.141	0.1554
2.5	2.513	0.2068
2.75	2.284	0.2156
3	2.094	0.2181
3.25	1.933	0.2165
3.5	1.795	0.2121
3.75	1.675	0.2060
4	1.570	0.1988
5	1.256	0.1656
6	1.047	0.1337
7	0.897	0.1062
8	0.785	0.0833
9	0.698	0.0643
10	0.628	0.0485
12	0.523	0.0243
14	0.448	0.0070
18	0.349	-0.0152

Table 5. Wavelength study for Re=44.984 and  $\sqrt{Ra}=100$  (case 1).

A linearized Navier-Stokes (LNS) simulation and a full Navier-Stokes (FNS) simulation for case 1 with 16 spanwise Fourier modes were then carried out for a spanwise domain extent of Z=12 (four times the most unstable wavelength). The mode amplitudes are plotted in Fig. 3. The growth rates are plotted in Fig. 4 and listed in Tab. 6. Mode k=4 (corresponding to  $\lambda_z=Z/4=3$  and  $\beta=2\pi/\lambda_z=2.094$ ) exhibits the strongest linear growth,  $\omega_i=0.2181$  (Fig. 3a). Modes 1-3 and 5-7 are also amplified in accordance with Fig. 2. This is a good example for the utility of the linearized code. The stability of several modes can be investigated with one simulation since the modes are not interacting with each other. The same case (case 1) was also simulated with the FNS code in order to validate the results obtained from the linearized Navier-Stokes (LNS) simulation. In accordance with the LNS simulation, mode k=4 exhibits the strongest

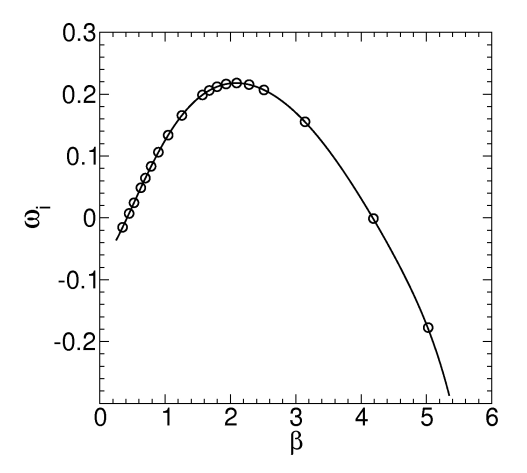


Figure 2. Growth rate versus spanwise wavenumber and polynomial curve fit for case 1 with varying Z and kmax=2.

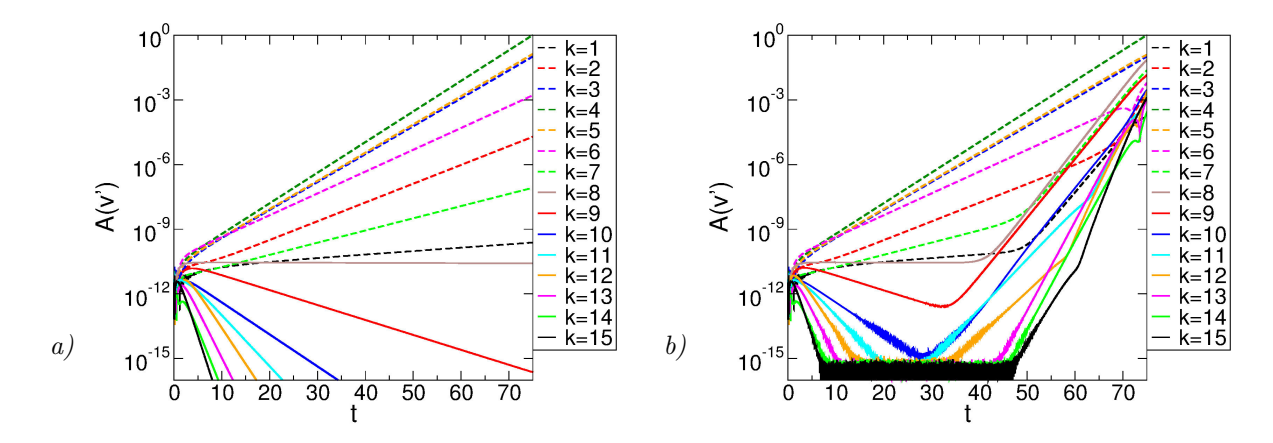


Figure 3. Mode amplitudes versus time for case 1 with fixed Z = 12 and kmax = 16: (a) LNS and (b) FNS.

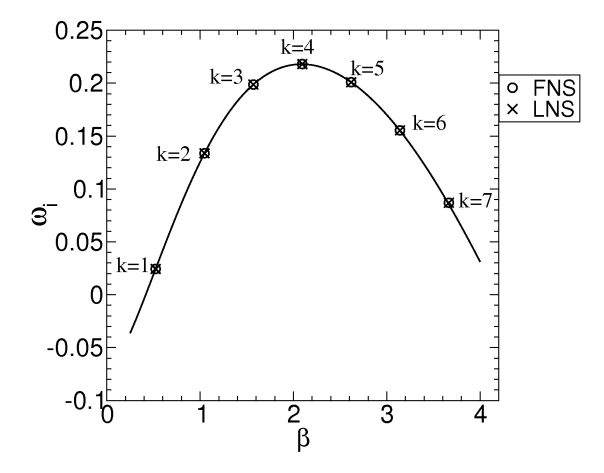


Figure 4. Growth rates versus spanwise wavenumber for case 1 and polynomial curve fit.

linear growth (Fig. 3b). The growth rates for t < 35 (linear growth) are in excellent quantitative agreement with the LNS results (Fig. 4).

k	$\lambda_z$	β	$\omega_i$
1	12	0.523	0.02439
2	6	1.047	0.1337
3	4	1.570	0.1988
4	3	2.094	0.2181
5	2.4	2.617	0.2009
6	2	3.141	0.1554
7	1.714	3.665	0.0869
8	1.5	4.1887	-0.00107
9	1.333	4.712	-0.1064
10	1.2	5.235	-0.228
11	1.09	5.759	-0.3644
12	1	6.283	-0.5153
13	0.923	6.806	-0.680
14	0.857	7.33	-0.857
15	0.8	7.853	-1.0511

Table 6. Spanwise wavelengths and wavenumbers as well as growth rates for case 1.

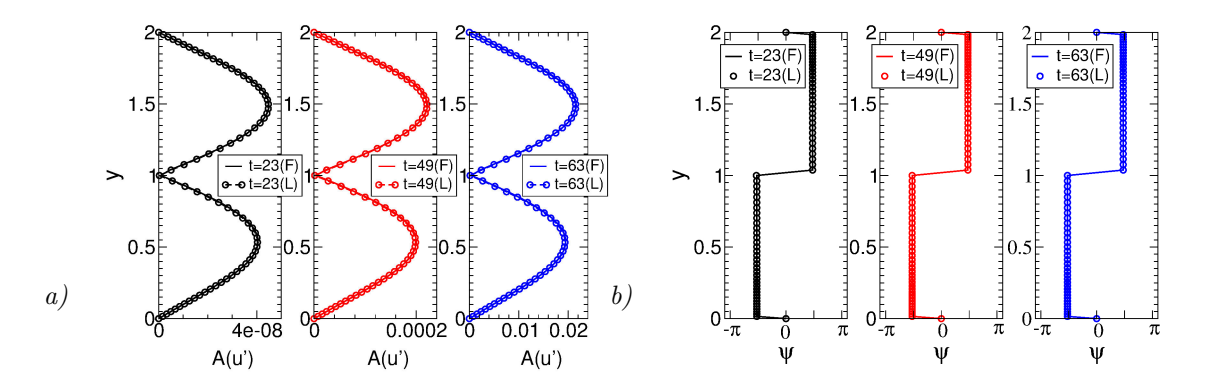


Figure 5. (a) Amplitude and (b) phase of u' for k=4 (case 1).

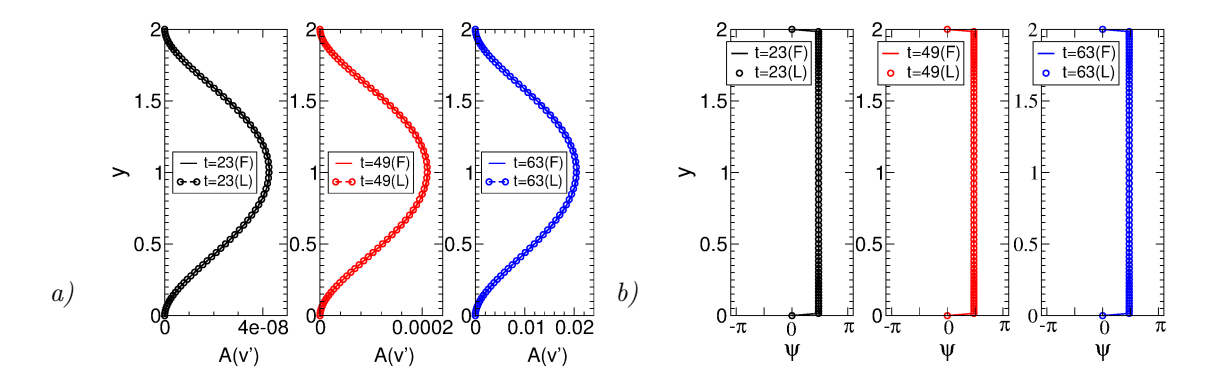


Figure 6. (a) Mode amplitude and (b) phase of v' for k=4 (case 1).

The amplitude and phase distributions of the streamwise disturbance velocity, u', for mode k=4 (case 1) for t=23, 49 and 63 are compared in Fig. 5. The amplitude distributions have two peaks and a phase-jump of  $\pi$  for  $y\approx 1$ . The amplitude and phase distributions of the wall-normal disturbance velocity, v' for mode k=4 are compared in Fig. 6. Unlike for the u' disturbance, only one amplitude peak exists at the mid-channel height (Fig. 6a) and the phase distribution is constant (Fig. 6b). Iso-surfaces of the Q-criterion<sup>38</sup> flooded by the streamwise vorticity and iso-contours of the wall-normal disturbance velocity obtained from the FNS simulation for t=75 reveal eight counter-rotating longitudinal vortices (Fig. 7).

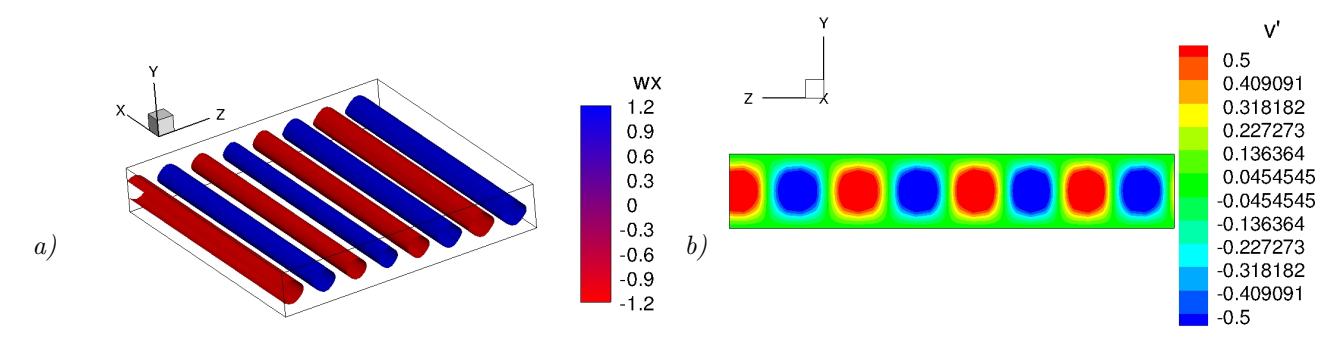


Figure 7. (a) Iso-surfaces of Q=2 flooded by streamwise vorticity and (b) iso-contours of v' for case 1.

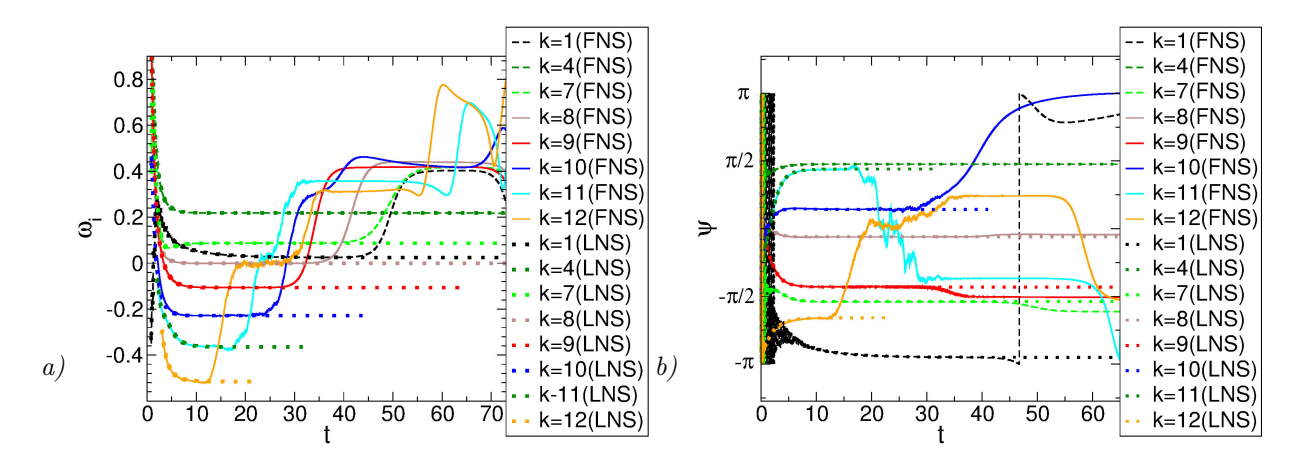


Figure 8. Comparison between FNS and LNS results: (a) Growth rate vs. time and (b) phase vs. time for case 1.

For the FNS simulation, the waves can interact and departures from linear growth are expected. Also, non-linear effects and amplitude saturation are possible. All Modes initially grow according to the linearized results (Fig. 8a). Sudden changes of the growth rate (such as for mode 8 for 40 < t < 50) can result from resonance or in general, non-linear effects. Mode k = 12 ( $\lambda_z = 1$ ) departs first from linear growth and is followed by modes k = 11, 10, 9, 8 and so on. Interestingly, the mode 12 non-linear growth levels of as mode 11 begins to grow. Similarly, the mode 11 growth tapers of as mode 10 starts to grow. A similar observation can be made for mode 10. Modes 9, 8, and 7 do not display this behavior. The non-linear growth of mode k = 8 ( $\lambda_z = 1.5$ ) is the strongest for 52 < t < 57 after which it is overtaken by mode 12. Sudden changes in growth rate go hand-in-hand with a phase adjustment of the modes (Fig. 8b). For example, the suddenly increased growth of mode 9 for t > 30 can be associated with a phase shift with respect to mode 4 that likely results in an improved non-linear energy transfer.

The amplitude and phase distributions of the streamwise and wall-normal disturbance velocity for mode k=7 are plotted in Figs. 9 and 10 for t=30 (linear growth), 48 (departure from linear growth) and 63 (constant non-linear  $\omega_i$ ). As the growth rate changes from t=30 to 63, the u' phase becomes flat and the v' phase attains a phase-jump of  $\pi$ . The u' amplitude distribution looses a peak whereas the v' amplitude distribution gains an extra peak. A similar scenario can also be observed for mode k=9 as seen in Figs. 11 and 12.

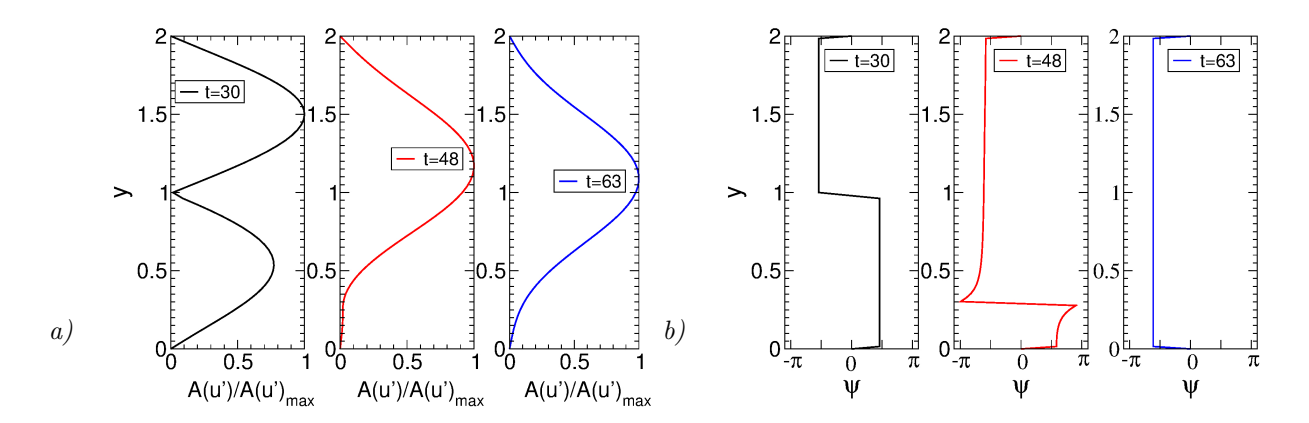


Figure 9. (a) Amplitude and (b) phase of u' for k = 7 (case 1).

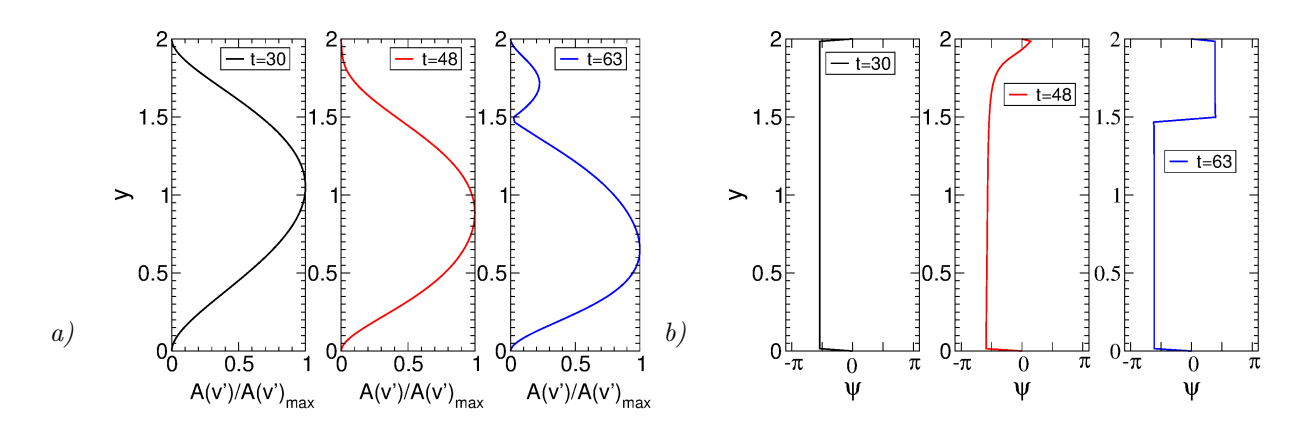


Figure 10. (a) Mode amplitude and (b) phase of v' for k = 7 (case 1).

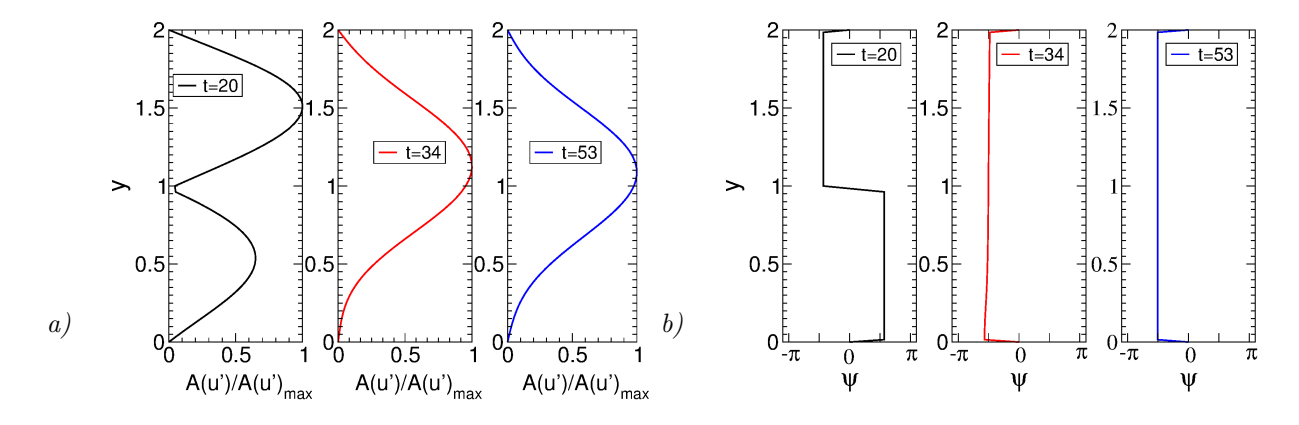


Figure 11. (a) Amplitude and (b) phase of u' for k = 9 (case 1).

Case 2 (Re = 30 and  $\sqrt{Ra} = 30$ ) is stable according to Gage and Reid.<sup>10</sup> Time histories of the disturbance amplitudes reveal that this is also the case for the simulation (Fig. 13).

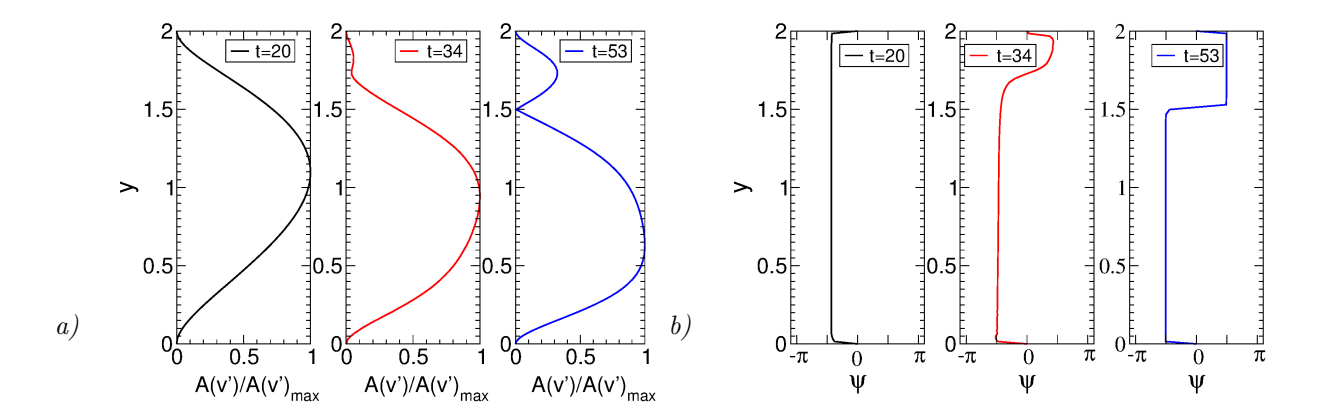


Figure 12. (a) Amplitude and (b) phase of v' for k = 9 (case 1).

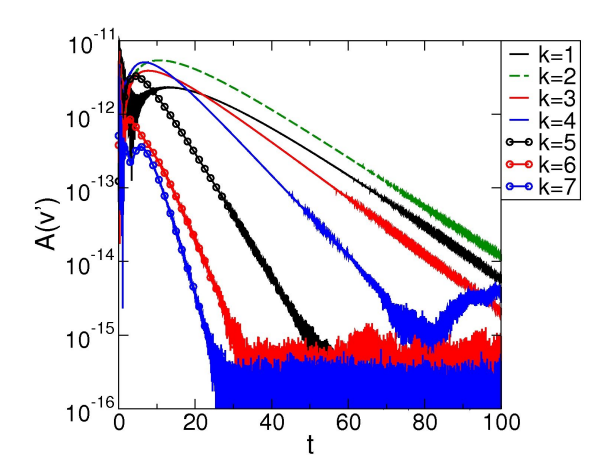


Figure 13. Time history of disturbance amplitudes for case 2.

## B. Viscosity-Driven Instability

The same approach was taken to investigate the viscosity-driven instability. The Rayleigh number ( $\sqrt{R}a = 10 < \sqrt{R}a_c$ ) was sub-critical and held constant. The Reynolds number was varied (Re=30,008.037 & 4,500.262). According to Gage and Reid, <sup>10</sup> 2-D disturbances in the form of Tollmien-Schlichting (T-S) waves are amplified for  $Re > Re_c = 5,400$ . The objective was to investigate the impact of the Reynolds number on the linear and non-linear stability for  $\sqrt{R}a < \sqrt{R}a_c$ . As for the bouyancy-driven instability, a grid resolution study was carried out first for Re = 30,008.037,  $\sqrt{R}a=10$ , and L=7 using LNS simulations with two streamwise Fourier modes (l=0 and l=1). The number of wall-normal grid points, J, was varied. Based on the grid resolution study (Tab. 7) it was decided to use 264 grid points in the wall-normal direction for all of the viscosity-driven instability simulations.

Using lmax=2, a wavelength study was conducted for the same parameters. The streamwise domain extent was varied to find the streamwise wavenumber,  $\alpha_r$ , with the highest temporal growth rate. In Tab. 8 and Fig. 14, the temporal growth rates,  $\omega_i$ , and frequencies,  $\omega_r$ , are provided for different wavelengths,  $\lambda_x$ , and wavenumbers,  $\alpha_r$ . The largest growth rate ( $\omega_i$ =0.00681) is obtained for a streamwise wavenumber of  $\alpha_r=2\pi/\lambda_x=0.837$  which corresponds to  $\lambda_x=7.5$  (Tab. 8 and Fig. 14a). Interestingly, this growth rate is roughly 30 times smaller than the maximum growth rate for the previous case with buoyancy-driven instability. Of course, this will change when the Reynolds number is increased. The phase speed for the most unstable mode is 0.1831. The frequency,  $\omega_r$ , and phase speed, c, increase with the wavenumber,  $\alpha_r$  (Tab. 8 and Fig. 14b).

J	$\omega_i$
48	0.01600
72	0.01083
96	0.00716
120	0.00602
144	0.00587
168	0.00591
192	0.00596
216	0.00599
240	0.00602
264	0.00603
288	0.00604
312	0.00604

Table 7. Grid resolution study for Re=30008.037 and  $\sqrt{R}a=10$ .

$\lambda_x$	$\alpha_r$	$\omega_i$	$\omega_r$	c
6	1.047	-0.00380	0.2106	0.2011
6.25	1.005	0.00018	0.1997	0.1987
6.5	0.966	0.00299	0.1891	0.1957
6.7	0.937	0.00456	0.1811	0.1932
7	0.897	0.00603	0.1699	0.1894
7.25	0.866	0.00663	0.1613	0.1862
7.5	0.837	0.00681	0.1533	0.1831
7.75	0.810	0.00667	0.1459	0.1801
8	0.785	0.00630	0.1390	0.1770
8.25	0.761	0.00575	0.1326	0.1742
8.5	0.739	0.00507	0.1267	0.1714
9	0.698	0.00346	0.1161	0.1663
10	0.6283	-0.00009	0.0988	0.1572

Table 8. Wavelength study with lmax = 2 for Re=30008.037 and  $\sqrt{Ra} = 10$  (case 3).

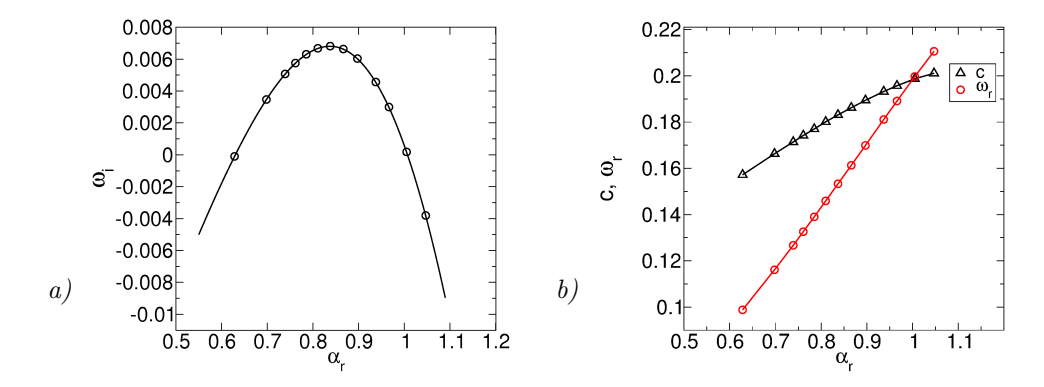


Figure 14. (a) Growth rate and polynomial curve fit and (b) frequency and phase speed versus streamwise wavenumber for Re=30008.037,  $\sqrt{R}a=10$ , and lmax=2 (case 3).

The streamwise domain extent was then set to four times the wavelength of the most amplified wave  $(L=4\times7.5=30)$ . Using 16 streamwise Fourier modes, this case was analyzed with the FNS and LNS code. For the LNS simulation, in agreement with the earlier wavelength study, mode l=4 grows linearly, mode l=3 is almost neutral, and mode l=5 is weakly damped (Fig. 15a). All other modes are decaying. Up to t=400 the FNS results match the LNS results. The first mode to grow non-linearly is l=8 ( $\lambda_x=3.75$ ) followed by mode l=12 ( $\lambda_x=2.5$ ) as seen in Fig. 15b. The growth rates for modes l=4, 8, and 12 are plotted in Fig. 19. As for the buoyancy-driven instability, the non-linear growth rates (e.g. k=8 and k=12) are larger than the linear growth rates (e.g. k=4). The wavelengths, wavenumbers, frequencies, phase speeds and growth rates for some of the modes are provided in Tab. 9.

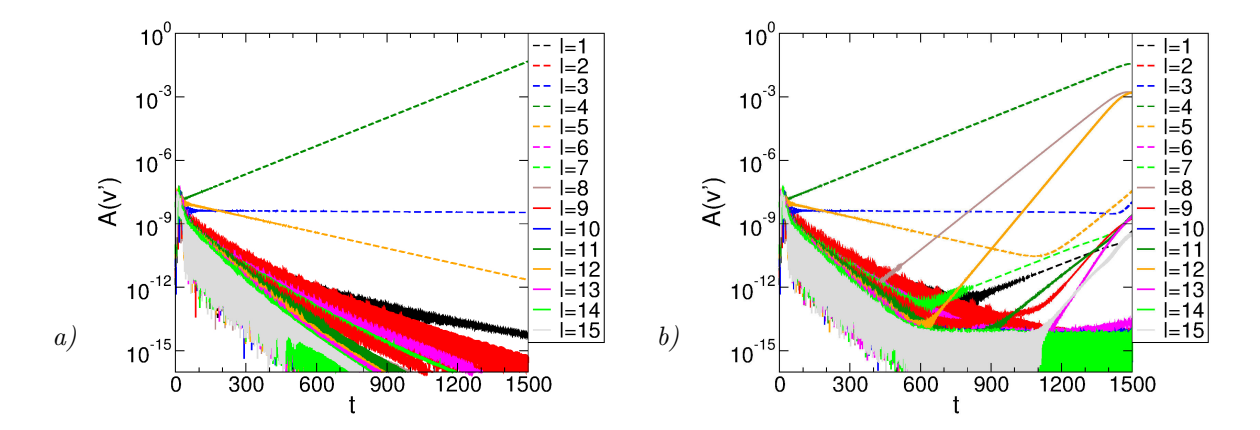


Figure 15. Mode amplitudes vs. time for case 3 with lmax = 16: (a) LNS and (b) FNS.

l	$\lambda_x$	$\alpha_r$	$\omega_r$	c	$\omega_i$
4 (linear growth)	7.5	0.837	0.1533	0.1831	0.00681
8 (non-linear growth)	3.75	1.675	0.3066	0.18304	0.01362
12 (non-linear growth)	2.5	2.513	0.46008	0.18308	0.02042

Table 9. Streamwise wavelength & wavenumber, frequency, phase speed and growth rate for case 3.

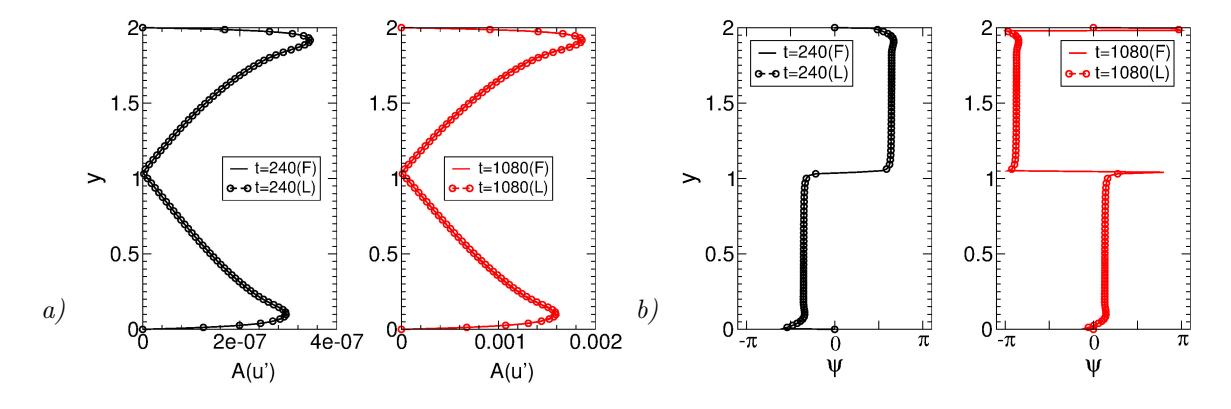


Figure 16. (a) Amplitude and (b) phase of u' for l=4 (case 3).

The u' and v' amplitude and phase distribution of mode l=4 for t=240 and 1080 are plotted in Figs. 16 and 17. As is typical for T-S waves, the u' mode amplitude has maxima near the top and bottom wall where the viscous affects are stronger (Fig. 16a) and a phase shift of  $\pi$  occurs at  $y \approx 1$  (Fig. 16b). On the

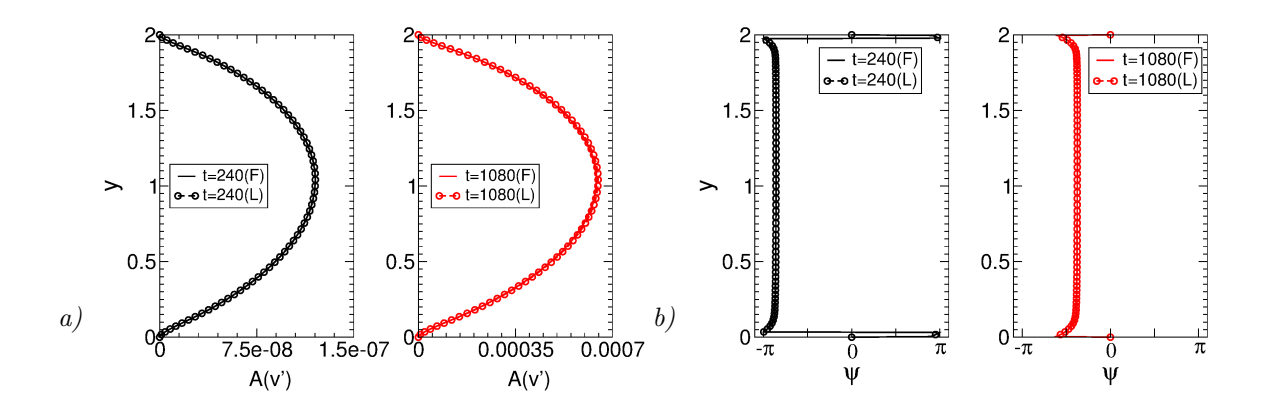


Figure 17. (a) Mode amplitude and (b) phase of v' for l = 4 (case 3).

other hand, the v' mode amplitude has only one peak at approximately the mid-channel height (Fig. 17a) and the phase remains constant inside the channel (Fig. 17b). Iso-contours of the disturbance velocity (v') obtained from the LNS simulation for t=1,500 are plotted in Fig. 18. The flow visualization shows one T-S wave.

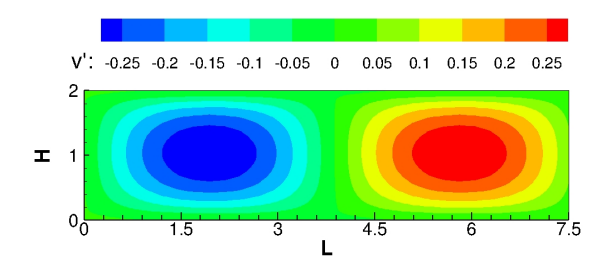


Figure 18. Iso-contours of wall-normal disturbance velocity for case 3 ( $\lambda_x = 7.5$ )

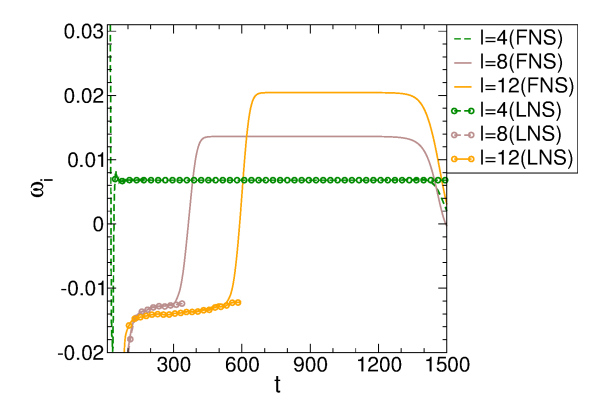


Figure 19. Growth rates versus time for case 3.

Modes l=8 and l=12 grow linearly up to  $t\approx 275$  and  $t\approx 500$  after which the growth rates increase strongly due to non-linear effects (Fig. 19). To better understand this phenomenon, the amplitude and phase of the streamwise and wall-normal disturbance velocity for mode l=8 were plotted for t=240 (linear growth), 360 (departure from linear growth) and 900 (non-linear growth) (Figs. 20 and 21). The u' disturbance amplitude distribution adjusts strongly as the non-linear effects set in. Two pronounced

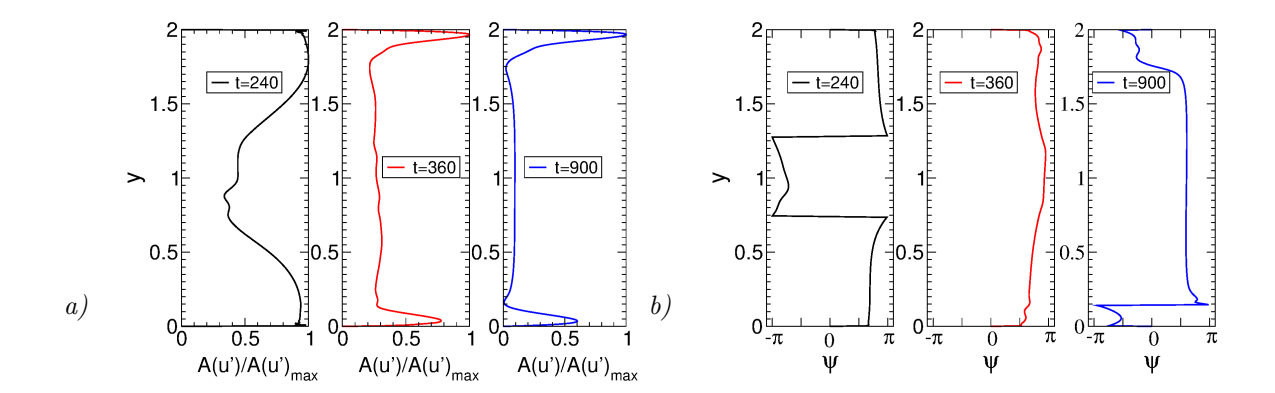


Figure 20. (a) Mode amplitude and (b) phase of u' for l = 8 (case 3).

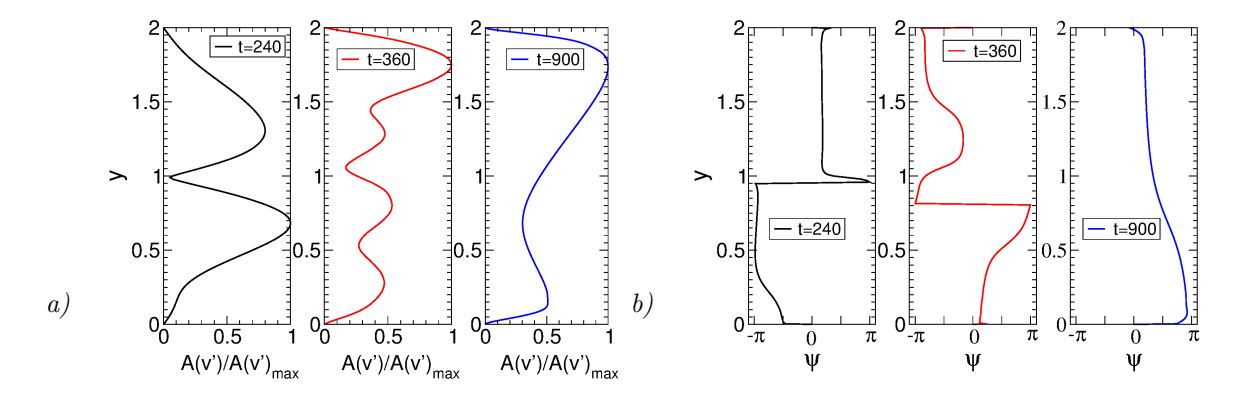


Figure 21. (a) Mode amplitude and (b) phase of v' for l = 8 (case 3).

near-wall maxima develop and one phase-jump is eliminated (Fig. 20). For the v' disturbance amplitude distribution, the amplitude peaks shift closer to the top and bottom wall and the phase-jump disappears (Fig. 21).

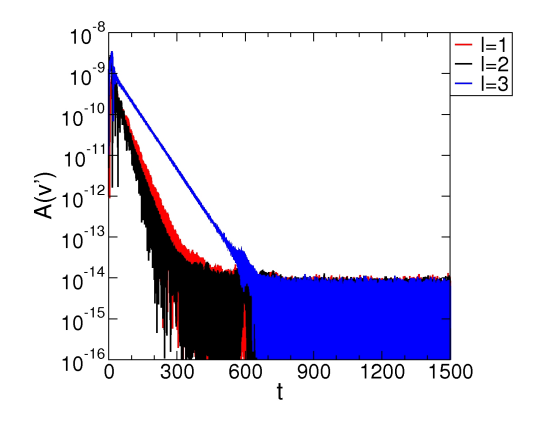


Figure 22. Mode amplitudes versus time for case 4.

Finally, for case 4 ( $Re = 4,501.626 < Re_c$ ), which is stable according to Gage and Reid, 10 all mode

## V. Conclusions

The plane Rayleigh-Bénard-Poiseuille flow can exhibit both buoyancy and viscosity-driven instability. Gage and Reid<sup>10</sup> were the first to provide neutral curves for plane RBP flow. According to Gage and Reid,<sup>10</sup> buoyancy-driven instability occurs when the Reynolds number is below  $Re_c$ =5,400 and the Rayleigh number is above  $Ra_c$ =1,708. In addition, viscosity-driven (Tollmien-Schlichting) instability occurs for  $Re > Re_c$  and  $Ra < Ra_c$ . The most unstable waves are three-dimensional (3-D) for the former and two-dimensional (2-D) for the latter. Gage and Reid<sup>10</sup> also provided neutral curves for 3-D oblique waves. The objective of this paper was to investigate both instabilities separately from each other.

To serve this objective, a linearized Navier-Stokes (LNS) and a full Navier-Stokes (FNS) code were developed for numerical stability investigations of RBP flows. The base flow profiles for the stability simulations were obtained from numerical solutions of the one-dimensional governing equations. As a validation case, the temporal stability results by Orszag<sup>27</sup> were recomputed and matched with good accuracy. The buoyancydriven instability was investigated for a subcritical Reynolds number and an unstable  $(Ra > Ra_c)$  and stable Rayleigh number. For the unstable case, the wavelength of the disturbances with the highest growth rate was obtained first with the LNS code. Linearized and full Navier-Stokes stability simulations were then carried out using a computational domain with a spanwise extent of four times the wavelength of the most unstable mode. Fourier transforms of the wall-normal disturbance velocity provided the mode amplitude and phase distribution and temporal growth rates as a function of the wavelength. Linear growth was observed for a wide range of spanwise wavenumbers,  $\beta$ . The FNS simulation revealed the onset of non-linear growth for a higher harmonic with a three times shorter wavelength relative to the most amplified linear wave. The onset of non-linearity is characterized by a phase-shift (the waves realign in the spanwise direction) and an additional zero-crossing of the mode amplitude distribution. As time progresses, an almost gradual reduction of the wavelength of the disturbances with the highest non-linear growth rate was observed. It may be speculated that 3-D disturbances would experience stronger non-linear growth. However, this is beyond the scope of this paper.

A subcritical Rayleigh number was chosen for the investigation of the viscosity-driven instability. Stability simulations were carried out for an unstable,  $Re > Re_c$ , and a stable Reynolds number. For the former, the streamwise wavelength of the disturbance waves with the highest temporal growth rate was determined first. The LNS simulations indicate that for a Reynolds number that is about six times higher than the critical Reynolds number, the unstable wavenumber range is quite narrow and the maximum amplification rates are roughly 30 times lower than for the case with buoyancy-driven instability where the Rayleigh number is approximately six times larger than the critical Rayleigh number. Because of the lower amplification rates and narrow wavenumber range, non-linear effects set in much later than for the cases with buoyancy-driven instability. Waves with two and three times shorter wavelength (relative to the linearly most amplified mode) are the first to experience non-linear growth. Three-dimensional waves may encounter stronger non-linear growth but were not investigated. For the conditions considered here, buoyancy-driven instability will likely first lead to transition. Non-linear interactions between the buoyancy and viscosity-driven instabilities will be discussed in a forthcoming paper.

## Acknowledgments

This material is based upon work supported by the National Science Foundation under grant no. 1510179. The program manager is Dr. Ronald Joslin.

## References

<sup>1</sup>Fasel, H., Meng, F., Shams, E., and Gross, A., "CFD analysis for solar chimney power plants," *Solar Energy*, Vol. 98, 2013, pp. 12-22

<sup>2</sup>Hasan, M.K., and Gross, A., "Numerical Investigation of Radial Flow in Solar Chimney Power Plant Collector," AIAA-Paper AIAA 2017-1010, 2017

<sup>3</sup>Braaten, M.E., and Patankar, S.V., "Analysis of laminar mixed convection in shrouded arrays of heated rectangular blocks," *International Journal of Heat and Mass Transfer*, Vol. 28, 1985, pp. 1699-1709

<sup>4</sup>Hasnaoui, M., Bilgen, E., Vasseur, P., and Robillard, L., "Mixed convective heat transfer in a horizontal channel heated

periodically from below," Numerical Heat Transfer, Part A, Vol. 20, 1991, pp. 297-315

<sup>5</sup>Zhang, S.Q., and Tangborn, A.V., "Flow regimes in two-dimensional mixed convection with spatially periodic lower wall heating," *Physics of Fluids*, Vol. 6, 1994, pp. 3285-3293

<sup>6</sup>Jensen, K.F., Einset, E.O., and Fotiadis, D.I., "Flow phenomena in chemical vapor deposition of thin films," *Annual Review of Fluid Mechanics*, Vol. 23, 1991, pp. 197-233

<sup>7</sup>Evans, G., and Greif, R., "Thermally unstable convection with applications to chemical vapor deposition channel reactors," *International Journal of Heat and Mass Transfer*, Vol. 36, 1993, pp. 2769-2781

<sup>8</sup>Ingle, N.K., and Mountziaris, T.J., "The onset of transverse recirculations during flow of gases in horizontal ducts with differentially heated lower walls," *Journal of Fluid Mechanics*, Vol. 277, 1994, pp. 249-269

<sup>9</sup>Nicola, X., Benzaoui, A., and Xin, S., "Numerical simulation of thermoconvective flows and more uniform depositions in a cold wall rectangular APCVD reactor," *Journal of Crystal Growth*, Vol. 310, 2008, pp. 174-186

<sup>10</sup>Gage, K.S., and Reid, W.H., "The stability of thermally stratified plane Poiseuille flow," Journal of Fluid Mechanics, Vol. 33, part I, 1968, pp. 21-32

<sup>11</sup>Miles, J.W., "On the stability of heterogeneous shear flows," Journal of Fluid Mechanics, Vol. 10, No. 4, 1961, pp. 496-508

<sup>12</sup>Pearlstein , A.J., "On the two-dimensionality of the critical disturbances for stratified viscous plane parallel shear flows," Physics of Fluids, Vol. 28, No. 2, 1985, pp. 751-753

<sup>13</sup>Ng , B.S., and Reid, W.H., "Instabilities in plane Poiseuille flow due to the combined effects of stratification and viscosity," *Physics of Fluids*, Vol. 9, No. 6, 1997, pp. 1844-1846

<sup>14</sup>Fujimura , K., and Kelly, R.E., "Interaction between longitudinal convection rolls and transverse waves in unstably stratified plane Poiseuille flow," *Physics of Fluids*, Vol. 7, No. 1, 1995, pp. 68-79

<sup>15</sup>Fujimura , K., and Kelly, R.E., "Stability of unstably stratified shear flow between parallel plates," *Fluid Dynamics Research*, Vol. 2, No. 4, 1988, pp. 281-292

<sup>16</sup>Akiyama, M., Hwang, G.J., and Cheng, K.C., "Experiments on the onset of longitudinal vortices in laminar forced convection between horizontal plates," *Journal of Heat Transfer*, Vol. 93, 1971, pp. 335-341

<sup>17</sup>Fukui, K., and Nakajima, M., "The longitudinal vortex and its effects on the transport processes in combined free and forced laminar convection between horizontal and inclined parallel plates," *International Journal of Heat and Mass Transfer*, Vol. 26, No. 1, 1983, pp. 109-120

<sup>18</sup>Hasan, M.K., and Gross, A., "Numerical Investigation of Hydrodynamic Stability of Inward Radial Rayleigh-Bénard-Poiseuille Flow," AIAA-Paper AIAA 2018-0586, 2018

<sup>19</sup>Luijkx, J.-M., Platten. J.K. and Legros, J.C., "On the existence of thermoconvective rolls, transverse to a superimposed mean Poiseuille flow," *International Journal of Heat and Mass Transfer*, Vol. 24, 1981, pp. 1287-1291

<sup>20</sup>Nicolas, X., Luijkx, J.-M., and Platten. J.-K., "Linear stability of mixed convection flows in horizontal rectangular channels of finite transversal extension heated from below," *International Journal of Heat and Mass Transfer*, Vol. 43, 2000, pp. 589-610

<sup>21</sup>Grandjean, E., and Monkewitz, P., "Experimental investigation into localized instabilities of mixed Rayleigh-Bénard-Poiseuille convection," *International Journal of Heat and Mass Transfer*, Vol. 24, 1981, pp. 1287-1291

<sup>22</sup>Mori , Y., and Uchida, Y., "Forced convective heat transfer between horizontal flat plates," *International Journal of Heat and Mass Transfer*, Vol. 9, No. 8, 1966, pp. 803-808

<sup>23</sup>Kachanov, Y.S., "Physical mechanisms of laminar-boundary-layer transition," Annual Review of Fluid Mechanics, Vol. 26, 1994, pp. 411-482

<sup>24</sup>Boiko, A.V., Westin, K.J.A., Klingmann, B.G.B., Kozlov, V.V., and Alfredsson, P.H., "Experiments in a boundary layer subjected to free stream turbulence. Part 2. The role of TS-waves in the transition process," *Journal of Fluid Mechanics*, Vol. 281, 1994, pp. 219-245

<sup>25</sup>Kachanov, Y.S., Kozlov, V.V., and Levchenko, V.Y., "Occurrence of Tollmien-Schlichting waves in the boundary layer under the effect of external perturbations," *Fluid Dynamics*, Vol. 13, No. 5, 1978, pp. 704-711

<sup>26</sup>Tam, C.K.W., "The excitation of Tollmien-Schlichting waves in low subsonic boundary layers by free-stream sound waves," *Journal of Fluid Mechanics*, Vol. 109, 1981, pp. 483-501

<sup>27</sup>Orszag, S.A., "Accurate solution of the Orr-Sommerfeld stability equation," *Journal of Fluid Mechanics*, Vol. 50, No. 4, 1971, pp. 689-703

<sup>28</sup>Nishioka, M., Iida, S., and Ichikawa, Y., "An experimental investigation of the stability of plane Poiseuille flow," *Journal of Fluid Mechanics*, Vol. 72, No. 4, 1975, pp. 731-751

<sup>29</sup>Lee, C., Min, T., and Kim, J., "Stability of a channel flow subject to wall blowing and suction in the form of traveling wave," *Physics of Fluids*, Vol. 20, 2008, pp. 101513(1-8)

<sup>30</sup>Chung, Y.M., Sung, H.J., and Boiko, A.V., "Spatal simulation of the instability of channel flow with local suction/blowing," *Physics of Fluids*, Vol. 9, No. 11, 1997, pp. 3258-3266

<sup>31</sup>Fan, P., "The standard upwind compact difference schemes for incompressible flow simulations," *Journal of Computational Physics*, Vol. 322, 2016, pp. 74-112

<sup>32</sup>Shukla, R.K., Tatineni, M., and Zhong, X., "Very high-order compact finite difference schemes on non-uniform grids for incompressible Navier-Stokes equations," *Journal of Computational Physics*, Vol. 224, 2007, pp. 1064-1094

<sup>33</sup>Sorensen, H., Jones, D., Heideman, M., and Burrus, C., "Real-valued fast Fourier transform algorithms," *IEEE Transactions ASSP*, Vol. 35, No. 6, June 1987, pp. 849-864

<sup>34</sup>Mitra, S.J., and Kaiser, J.F., "Digital Signal Processing Handbook," Chap. 8, 1993, John Wiley & Sons, pp. 491-610

<sup>35</sup>Fyfe, D.J., "Economical Evaluation of Runge-Kutta Formulae," Mathematics of Computation, Vol. 20, 1966, pp. 392-398

<sup>36</sup>Thomas, L.H., "The stability of plane Poiseuille flow," Physical Review, Vol. 91, No. 4, 1953, pp. 780-783

 $^{37}$ Gary, J., and Helgason, R., "A matrix method for ordinary differential eigenvalue problems," *Journal of Computational Physics*, Vol. 5, 1970, pp. 169-187

<sup>38</sup> Hunt, J.C.R., Wray, A.A., and Moin, P., "Eddies, stream and convergence zones in turbulent flows," *Report CTR-S88*, Center for Turbulence Research, Stanford, CA, 1988